Impact of valley phase and splitting on readout of silicon spin qubits

M. L. V. Tagliaferri, P. L. Bavdaz, W. Huang, A. S. Dzurak, D. Culcer, and M. Veldhorst

Impact of valley phase and splitting on readout of silicon spin qubits

M.L.V.Tagliaferri,[1, *] P.L. Bavdaz,[1] W. Huang,[2] A.S. Dzurak,[2] D. Culcer,[3, 4] and M. Veldhorst[1, †]

[1]*QuTech, TU Delft and Kavli Institute of Nanoscience, PO Box 5046, 2600GA, Delft, The Netherlands*
[2]*Centre for Quantum Computation and Communication Technology,*
School of Electrical Engineering and Telecommunications,
The University of New South Wales, Sydney 2052, Australia
[3]*School of Physics, The University of New South Wales, Sydney 2052, Australia*
[4]*ARC Centre of Excellence in Future Low-Energy Electronics Technologies, Sydney 2052, Australia*

We investigate the effect of the valley degree of freedom on Pauli-spin blockade readout of spin qubits in silicon. The valley splitting energy sets the singlet-triplet splitting and thereby constrains the detuning range. The valley phase difference controls the relative strength of the *intra-* and *inter-* valley tunnel couplings, which, in the proposed Pauli-spin blockade readout scheme, couple singlets and polarized triplets, respectively. We find that high conversion fidelity is possible for a wide range of phase differences, while taking into account experimentally observed valley splittings and tunnel couplings. We also show that the control of the valley splitting together with the optimization of the readout detuning can compensate the effect of the valley phase difference. To increase the measurement fidelity and extend the relaxation time we propose a latching protocol that requires a triple quantum dot and exploits weak long-range tunnel coupling. These opportunities are promising for scaling spin qubit systems and improving qubit readout fidelity.

I. INTRODUCTION

The experimental demonstration of high-fidelity quantum dot qubits with long-coherence[1,2] that can be coupled to perform two-qubit logic gates[3,4] and used to execute small quantum algorithms[5] has positioned silicon as a promising platform for large-scale quantum computation. Building upon these advances, exciting new directions forward have been proposed[6–13], that exploit uniformity[14], robustness against thermal noise[15], or semiconductor manufacturing[16], and aim for operation of quantum error correction codes[17] on qubit arrays.
Despite its promises, silicon poses specific challenges due to the six-fold degeneracy of its conduction band minimum in bulk. This degeneracy is lifted close to an interface, and a gap opens between perpendicular and in-plane valley doublets. Interfaces and gate electric fields cause coupling either in the same or different orbital levels. The same-doublet same-orbital coupling is the so-called valley mixing, while the others are generally referred to as valley-orbit coupling[18]. Whereas silicon quantum dots can often be operated in the regime of vanishingly small valley-orbit coupling[19–21], valley mixing can not be neglected. It has been shown[21–23] that this does not lead to a direct splitting between the bulk valleys, but the coupling gives rise to a valley splitting between the valley eigenstates. As a consequence, the valley mixing is determined by two parameters only[24]: its phase, the *valley phase*, and its modulus, the *valley splitting*. Typical valley splittings range from tens of neV to about 1 meV[1,25–28] and introduce new challenges for spin qubits defined in silicon quantum dots. Despite them, it has been shown that universal quantum computation with spin qubits is still possible[29]. On the contrary, consequences of valley phase have been studied only in limited research, but found to be significant in valley-qubits[30] and donors close to an interface[31], while they strongly

influence the exchange interaction[32]. A crucial question is therefore how much the valley mixing impacts quantum computation with spins in silicon quantum dots in the general case of non-negligible valley non-preserving tunnel coupling.
Here, we investigate its effect on readout, now one of the most challenging operations for spin qubits. We concentrate on Pauli-spin blockade readout and show that high spin-to-charge conversion fidelity is achievable in a wide parameter range. This readout technique is considered in large-scale quantum computation proposals[14–16] since it requires few electron reservoirs and is compatible with moderate magnetic fields[33,34]. However, in standard Pauli-spin blockade schemes the readout time is limited due to spin-relaxation[35–37]. Moreover, usually two spin states are projected on charge states with different the electric dipole, leading to a readout fidelity smaller than the conversion fidelity[38,39]. A possible solution is to exploit latching mechanisms in the pulsing scheme, locking the charge in a long-lived metastable state[40–42]. The final states now have a different number of electrons, improving the readout fidelity[39]. Here we overcome these limitations and propose a protocol based on a triple quantum dot, removing the need of an external reservoir.
This work is organized as follows. In Section II, we introduce the model describing a multi-valley two-electron double quantum dot and discuss Pauli-spin blockade readout. In Section III, we investigate how the valley phase difference and splitting energy impact the spin-to-charge conversion fidelity. We identify the conditions that enable conversion fidelities beyond 99.9%. A triple quantum dot scheme combining Pauli-spin blockade with long lived charge states is proposed and studied in Section IV. We discuss the conclusions and opportunities in Section V.
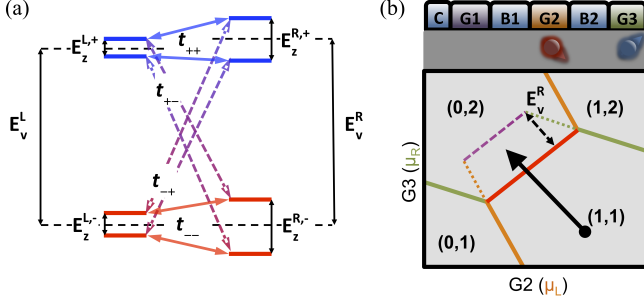
FIG. 1: (a) Spin-valley single-particle energy levels of a silicon double quantum dot. The valley ground states are shown in red, while the excited valley states, separated by the dot-dependent valley splitting $E_v^{L(R)}$, are in blue. A dot and valley-dependent Zeeman energy (e.g. $E_Z^{L,-}$) splits the spin states. The constant color arrows represent the intravalley tunnel coupling $t_{\pm\pm}$, while intervalley coupling $t_{\pm\mp}$ arrows have a color gradient. (b) Top: Cross-section of a schematic device. The confinement gate (C) defines the dots, plunger gates (G) accumulate the electrons and control the out-of-plane electric field, while the barrier gates (B) tune the tunnel coupling t. Bottom: Schematic stability diagram of a double quantum dot. Green and orange lines mark the dot-lead transitions. Interdot intervalley tunneling occurs along the dashed line, separated from the ground state line by the right dot valley splitting E_v^R.

II. MODEL

A. Silicon Double Quantum Dot Hamiltonian

The model developed in this Section can be generalized to other doubly occupied multi-valley double quantum dots, but here we restrict the discussion to quantum dots at the Si/SiO$_2$ interface. We define the left and right quantum dots as target and ancilla qubits respectively. We consider ten single-particle spin-valley states: the four lowest orbital spin-valley states of each dot shown in Fig. 1a and the two lowest valley states in the first excited orbital of the ancilla qubit, needed to build the same-valley triplet states of the doubly occupied ancilla qubit. As shown in Fig. 1b, the double dot is tuned by means of two plunger gates (G), controlling the energy levels, and two barrier gates (B), setting the interdot tunnel coupling. Furthermore we assume a valley splitting energy $E_v = [100\,\mu\text{eV}, 1\,\text{meV}]$ and an orbital splitting energy close to 10 meV, consistent with experimentally measured values[1,26,27]. The order of magnitude larger orbital splitting, together with operation at a small magnetic field, justifies the assumption of a negligibly small valley orbit coupling and pure valley mixing[18,19,21].

Each dot is described by the Hamiltonian $H_0^d = H_v^d + H_Z^d + \delta_{d,R} H_o^R$, where $d = L, R$ is the dot label, H_v^d describes the valley spectrum of the dot, H_Z^d the Zeeman splitting and H_o^R the orbital levels of the right dot ($\delta_{d,R}$ is the Kronecker delta). In particular:

$$H_v^d = E_v^d \sum_{v=-,+} \delta_{v,+} \sum_{\substack{o=0,1 \\ \sigma=\downarrow,\uparrow}} c_{d,o,\atop v,\sigma}^\dagger c_{d,o,\atop v,\sigma} , \tag{1}$$

$$H_Z^d = \frac{1}{2} \sum_{\substack{o=0,1 \\ v=-,+}} E_Z^{d,v} (c_{d,o,\atop v,\uparrow}^\dagger c_{d,o,\atop v,\uparrow} - c_{d,o,\atop v,\downarrow}^\dagger c_{d,o,\atop v,\downarrow}) , \tag{2}$$

$$H_o^R = E_o^R \sum_{o=0,1} \delta_{o,1} \sum_{\substack{v=-,+ \\ \sigma=\downarrow,\uparrow}} c_{R,o,\atop v,\sigma}^\dagger c_{R,o,\atop v,\sigma} , \tag{3}$$

where o, v and σ are the orbital, valley and spin labels respectively. The Zeeman splitting is defined as $E_Z^{d,v} = g_{d,v}\mu_B B_d$. In general the g-factor is valley and dot dependent due to spin-orbit coupling[43,44]. Here we assume a vanishingly small spin-orbit coupling[45–47] arising from a magnetic field applied along one of the minimizing directions. This assumption is further warranted by the possibility of low magnetic field operation when using Pauli-spin blockade readout (low field operations has several other advantages, see Refs. 14,15). In this range, finite $\delta E_Z^v = E_Z^{R,v} - E_Z^{L,v}$ can be realized via nanomagnets, and we restrict to the case $E_Z^{R,v} > E_Z^{L,v}$. H_v describes the splitting between the valley eigenstates due to the mixing of the $k_{\pm z}$ bulk valleys induced by the Si/SiO$_2$ interface and the electric field[23,48,49]. We consider dot-dependent valley splittings[25] due to interface effects and local variations in electric field[19]. The valley coupling is $\Delta_v \equiv E_v e^{i\phi_D}$, whose modulus is the valley splitting energy and whose phase is the valley phase (i.e. the phase of the fast Bloch oscillations of the wave function)[50,51]. The valley eigenstates are of the form $D_\pm = (1/\sqrt{2})(D_z \pm e^{i\phi_D} D_{-z})$, where $D_{\pm z} = L_{\pm z}, R_{\pm z}$ are the bulk $\pm z$ valleys wavefunctions of the quantum dots[23,49].

The two-electron double-dot Hamiltonian reads:

$$H_{2e} = H_0 + H_\epsilon + H_C + H_t. \tag{4}$$

Here H_0 describes two non-interacting quantum dots. H_ϵ is the detuning term, describing the gate-controlled shift ϵ of the ancilla qubit energy levels with respect to those of the target qubit. Referring to Fig. 1b, this corresponds to increasing the voltage on G3. The third term H_C accounts for the effect of the Coulomb potential V_{ee}. For the system considered here and within the Hund-Mulliken approximation, the Coulomb exchange integral $j = \langle L_z R_{\pm z} | V_{ee} | R_z L_{\pm z} \rangle$ and the valley exchange integral $j_v = \langle D_{\mp z} D_{\pm z} | V_{ee} | D_{\pm z} D_{\mp z} \rangle$ are negligible[22,52,53]. Theoretical works have estimated $j \approx 1\,\mu\text{eV}$ for 30 nm separated dots[54] and $j_v \ll 1\,\mu\text{eV}$[22]. The on-site repulsion in the ancilla (right) dot $U_o^R = \langle R_v R_{v(\bar{v})} | V_{ee} | R_v R_{v(\bar{v})} \rangle$, or charging energy, is assumed to be a few tens of meV[26,27]. In the Pauli spin blockade readout scheme only the ancilla qubit can be doubly occupied, thus the $(2,0)$ states are neglected and hence terms of the form $\langle LL | V_{ee} | LL \rangle$ do not appear in H_C. The remaining two Coulomb integrals do not appear

explicitly in H_C since the direct Coulomb interaction $k = \langle L_z R_{\pm z} | V_{ee} | L_z R_{\pm z} \rangle$ is an offset, while the Coulomb interaction enhancement terms $s = \langle R_{\pm z} R_z | V_{ee} | L_{\pm z} R_z \rangle$ are part of the tunnel coupling t. It holds that $t = t_0 + s$, where $t_0 = \langle R_z | H_0 | L_z \rangle$. The last term in H_{2e} is the tunnel Hamiltonian expressing the hopping of one electron between the two dots. The different terms of the Hamiltonian are:

$$H_0 = \sum_{d=L,R} H_0^d \,, \tag{5}$$

$$H_\epsilon = -\epsilon \sum_{\substack{o=0,1 \\ v=-,+ \\ \sigma=\downarrow,\uparrow}} c^\dagger_{R,o,} c_{R,o,} \,, \tag{6}$$

$$H_C = \sum_{o=0,1} U_o^R \sum_{\substack{o'=0,1 \\ \sigma,\sigma'=\downarrow,\uparrow \\ v,v'=-,+}} n_{R,o,} n_{R,o',} \,, \tag{7}$$

$$H_t = \sum_{\substack{v,v' \\ o,o' \\ \sigma}} t_{vv'} c^\dagger_{R,o,} c_{L,o',} \prod_{\substack{r=v_R,\sigma_R,o_R \\ R=S,V,O}} (-1)^{\delta_{r,ES}\delta_{R,0}} + H.c. \,, \tag{8}$$

where n is the number operator, σ_R, v_R and o_R are the spin, valley and orbital indexes of the right electron and S, V, O are the spin, valley and orbital numbers of the two-electron state. The label ES stands for the excited state of the quantum number expressed by r. The condition $S(V, O) = 0$ means that the spin (valley or orbital) part of the 2-electron wavefunction is a spin singlet (valley or orbital) built from the single particle states. $t_{\pm\pm}$ and $t_{\pm\mp}$ are the intravalley and intervalley tunnel couplings, respectively[22,55,56]. The first(second) coupling allows for tunneling between valley eigenstates of the same(different) form. We note that both terms prevent tunneling between states that have a different bulk valley index[49]. It holds[22] that $t_{\pm\pm} = \frac{t}{2}[1 + e^{-i\Delta\phi}]$ and $t_{\pm\mp} = \frac{t}{2}[1 - e^{-i\Delta\phi}]$, where $\Delta\phi = \phi_L - \phi_R$ is the valley phase difference. The exact value of $\Delta\phi$ depends strongly on microscopic origins such as the interface roughness and the height difference between the dots. For instance, since $\phi = 2k_0 d$, where d is the distance from the interface, even a single terrace step ($d = a_0/4$) leads to a quite large phase difference[23] $\phi \approx 0.84\pi$. In the case of a negligibly small height difference and a flat interface the valley mixing is the same and the valley eigenstates have the same valley composition. In practice, however, typical quantum dots have an orbital spacing on the order of 10 meV, corresponding to a dot size of around 10 nm, which is comparable to the correlation length range (few to hundreds of nm) reported for the Si/SiO$_2$ interface[32]. As such, we expect different quantum dots to have different valley compositions.

B. Two-electron energy levels

Having considered 10 single-particle spin-valley states, the Hamiltonian H_{2e} is expressed on a 26-state basis. These are the twenty-two lower orbital states and four $(0,2)$ states describing the same-valley double occupancy of the ancilla qubit. However, these same-valley double occupancy states contribute significantly to the eigenstates only at high detuning (i.e. $\epsilon \gtrsim U^R + E_o^R$) and we neglect therefore higher energy $(0,2)$ states. The basis states are tensor products[49,57] of the form $|(\sigma_L, \sigma_R)\rangle |\psi_V\rangle |\psi_O\rangle$ and $|\chi_S\rangle |\psi_V\rangle |\psi_O\rangle$ for the $(1,1)$ and $(0,2)$ charge configurations. Here $|\chi_S\rangle$ is the two-spin wavefunction while $|\psi_V\rangle$ and $|\psi_O\rangle$ are the symmetrized two-particle valley and orbital functions. For simplicity, from here on the orbital part is dropped, while we label the $(0,2)$ states as $S_{(0,2)}^{v,v'}$, $T_{0,(0,2)}^{v,v'}$ or $T_{\pm,(0,2)}^{v,v'}$.

In this work, we consider the case when $E_v^R \gtrsim E_v^L > E_Z^{R,L}$ and, as shown in Fig. 2a three branches separated by the valley splitting emerge[49]: in the lowest $(--)$ and highest $(++)$ branch the two electrons have the same valley number, while in the middle branch they are opposite $(\pm\mp)$. The $(1,1)$ same-valley branches consist of four states each, while in the $(0,2)$ configuration these same states include only the spin singlet state, because of the Pauli exclusion principle. The different-valley branch includes eight levels when in the $(1,1)$ and four states in the $(0,2)$ charge states. The difference in Zeeman energy sets the energy splitting between the antiparallel spin states in the three branches. A small difference in valley splitting energy splits the $(+-)$ and $(-+)$ states, as shown in Fig. 2a. The control of $\Delta\phi$ allows to select the nature of interdot tunneling, ranging from intra- to intervalley-only tunneling, as shown in Fig. 2b. In particular, for $\Delta\phi = 0$ the $|\downarrow,\downarrow\rangle$ states are uncoupled from the $(0,2)$ charge states in the lowest orbital and the blocked region extends to the orbital spacing energy.

C. Two-dot Pauli-Spin Blockade readout

At negative detuning (i.e. $\epsilon \ll U^R$), the two lowest eigenstates can be approximated with the basis states $|\downarrow,\downarrow\rangle |--\rangle$ and $|\uparrow,\downarrow\rangle |--\rangle$. Differing only in the spin orientation of the target qubit, these states are hereafter used as initial states of the Pauli-spin blockade readout protocol and their valley label is dropped.

As shown in Fig. 2c, Pauli-spin blockade readout consists of a spin-to-charge conversion. At the beginning of the readout protocol, the ancilla qubit is in the ground state while the target qubit can be either spin up or spin down. The readout pulse detunes the double quantum dot beyond the intravalley anticrossing and inside the blocked region ($U^R < \epsilon_f < U^R + E_v^R - E_Z^{R,-}$), the brown region in Fig. 2c. As shown in Fig. 2d, if the two spins are initially
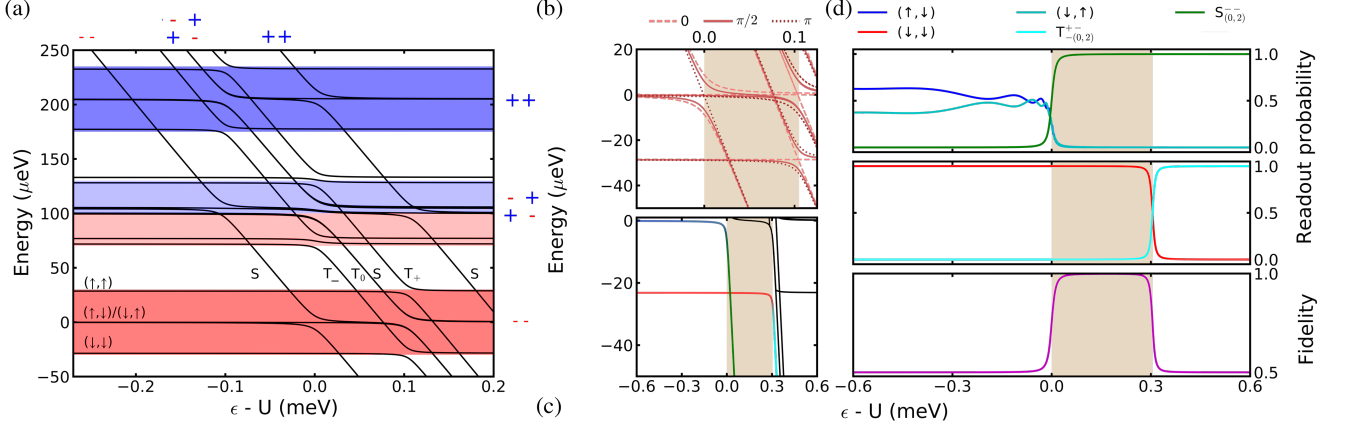
FIG. 2: (a) Energy levels of a multivalley double quantum dot with $E_v > E_Z$. We distinguish three separate branches of energy states: the valley ground states (red), the valley excited states (blue), and the valley mixed states (light blue and red). The difference in valley splitting causes the splitting between the $(+, -)$ and $(-, +)$ sub-branches. The simulation parameters were: $U_o^R = 30$ meV, $t = 1.5$ GHz, $\Delta\phi = \pi/2$, $E_v^{R(L)} = 105$ (100) μeV, $E_o^R = 10$ meV and $E_Z^{R(L),-} = 28.65$ (28.5) μeV. The two-spin states have a similar order for the three branches and are shown for the lowest branch only. (b) Zoom-in at the intravalley anticrossing. Increasing the phase difference from 0 to π changes the tunneling from pure intravalley to pure intervalley. The light brown rectangle highlights the high fidelity detuning range. c) Schematic of Pauli-spin blockade readout sequence. The states used in the readout protocol are shown with the same colors as in (d). The double quantum dot is initialised either in $|\uparrow,\downarrow\rangle$ (in blue) or $|\downarrow,\downarrow\rangle$ (in red). The detuning is consequently changed linearly with an adiabatic pulse. Here $E_v^{R(L)} = 300$ (305) μeV and $\delta E_Z^- = 20.7$ neV. (d) Results of time evolution simulations, using the same parameters as in (c). Inside the high fidelity region F is higher than 99.9%. The oscillations at negative detuning in the top panel are the fingerprint of a singlet $(1,1)$. The pulse starts at the symmetry point and the pulse duration is set to achieve a high degree of adiabaticity (See Appendix for more details).

antiparallel (blue level in Fig. 2c) the final state will be the singlet $S_{(0,2)}^{--}$ (green level); otherwise, the system will remain blocked in $|\downarrow,\downarrow\rangle$ (red level) until it relaxes via a spin flip. Experimentally, the final state can be probed either by charge sensing[33,34] or by gate based dispersive rf-readout[58]. However, these techniques require slightly different pulses. The former detects differences in the electric field due to a difference in the charge configuration, while the latter probes the level mixing via the quantum capacitance[59]. The highest fidelities are obtained far from or close to the intravalley anticrossing[60], respectively.

Here we consider 1 μs long linear adiabatic pulses conceived for charge sensing. (See the Appendix for details on pulse adiabaticity.) We note that shaped pulses could improve speed and performance (see Ref. 14 and therein references), although in arrays operated by shared control linear pulses could be required[14]. The duration is chosen as a trade off between fast pulses and adiabaticity. The conversion fidelity F is defined as the probability that $|\uparrow,\downarrow\rangle$ evolves to a $(0,2)$ state while $|\downarrow,\downarrow\rangle$ remains in a $(1,1)$ state. Since at the beginning of the readout protocol the system is either in one of the two lowest lying eigenstates with the same probability, the conversion fidelity is the weighted sum of $F_{|\uparrow,\downarrow\rangle\to(0,2)}$ and $F_{|\downarrow,\downarrow\rangle\to(1,1)}$:

$$F = \frac{F_{|\uparrow,\downarrow\rangle\to(0,2)} + F_{|\downarrow,\downarrow\rangle\to(1,1)}}{2}$$
$$= \frac{1}{2}\left[\sum_{a\in(0,2)} |\langle a|f\rangle|^2 + \sum_{b\in(1,1)} |\langle b|f'\rangle|^2\right], \quad (9)$$

where f and f' are the two final states calculated from the time evolution of the two lowest-lying eigenstates $|\uparrow,\downarrow\rangle$ and $|\downarrow,\downarrow\rangle$, respectively.

From Eq. 9 it can be seen that the ultimate limit to the readout fidelity is set by the final state composition, which depends on the valley phase difference. Even a perfectly adiabatic pulse results in $F < 1$ if the final state f' has a non negligible contribution from $T_{-,(0,2)}^{+-}$ (see Fig. 2a).

We recall that we have assumed negligible spin-orbit coupling. Contrarily to bulk silicon, in quantum dots defined at the Si/SiO$_2$ interface it can be non-negligible. The structural inversion asymmetry leads to a Rashba spin-orbit coupling, while the dominant Dresselhaus[47] arises from the interface inversion asymmetry[61–63]. The spin-orbit coupling strength depends, apart from the magnetic field orientation, on the vertical electric field, valley composition and the microscopic properties of the interface[44]. In actual devices it causes g-factor variability[45], valley dependency[43,46] and mixing between antiparallel and
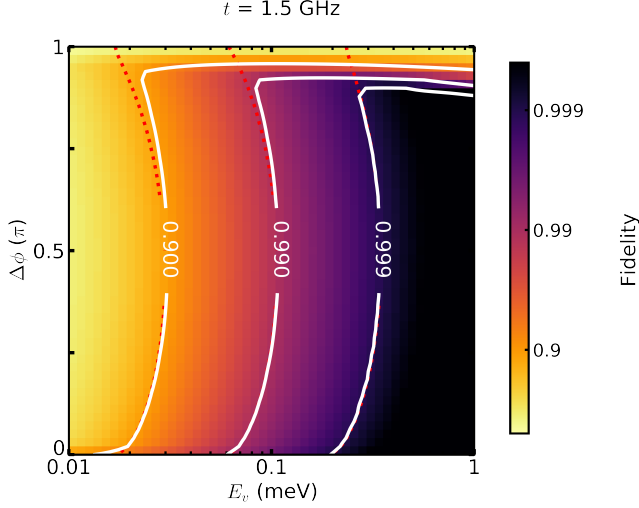
FIG. 3: Fidelity obtained by pulsing from $\epsilon = U^R - 1$ meV to $U^R + E_v^R$ in 1 μs with $\Delta t = 1$ ps, $t = 1.5$ GHz and $\delta E_Z^- = 5$ MHz, for a range of experimentally achieved valley splitting energies (here $E_v^R = E_v^L$). Contour lines are shown in white. The decrease in F for $\Delta\phi$ approaching π (i.e. $t_{\pm\pm} \to 0$) is caused by an increase in diabaticity, due to the constant pulse duration, absent in adiabatic evolution (red). For each point of the map, we have plotted the maximum achievable fidelity by taking the optimal detuning.
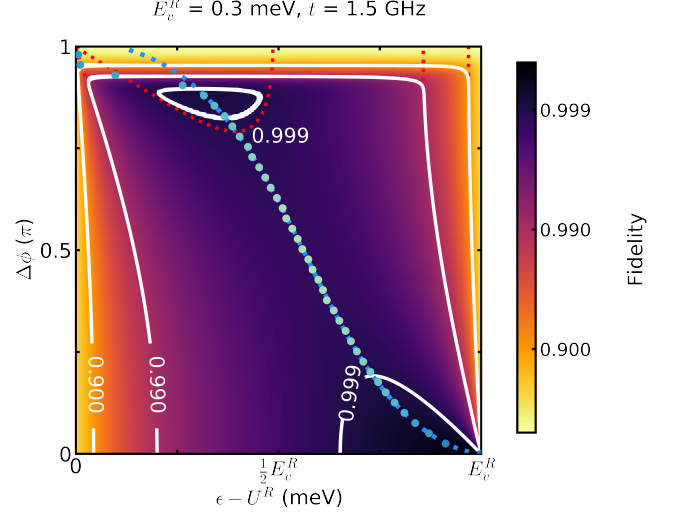
FIG. 4: Fidelity obtained by time evolution simulations (color map with white contour lines) and perfectly adiabatic pulses (red). The difference between the detuning position of maximum fidelity obtained from time evolutions simulations (dots) and adiabatic pulses (dashed line) is due to the finite speed of the pulse. As a consequence of the chosen parameters (e.g. $\delta E_Z^- = 5$ MHz, $E_v^R = 300$ μeV, $t = 1.5$ GHz and pulsing from $U^R - 2E_v^R$ to $U^R + 2E_v^R$) a gap where $F < 99.9\%$ opens for intermediate $\Delta\phi$. The maximum fidelity has a non-monotonic dependence on $\Delta\phi$, visualized here by the color map of the dots; a minimum is observed at $\pi/2$ (light green), a local maximum at π (blue), and the maximum at 0 (dark blue).

parallel spin states[64]. As a consequence, when including the spin-orbit Hamiltonian in H_{2e} anticrossings between $S_{(0,2)}^{--}$ and the polarized triplets emerge[38,44]. Further, such mixing would reduce F even for adiabatic pulses. The shape of the pulse used for Pauli-spin blockade readout has to be modified accordingly, i.e. a two-speed linear pulse, to allow for a diabatic crossing of the $S - T^-$ anticrossing[65]. Therefore our assumption of negligible spin-orbit coupling ensures that our results demonstrating the impact of valley phase are not obscured by spin-orbit effects.

III. RESULTS

From previous considerations, it emerges that the larger E_v^R the greater F. In general, E_v^R can be tuned via a vertical electric field[1,19,48]. In the device shown in Fig. 1b, valley splitting can be controlled via the combined tuning of G3 and confinement gate C.

In Fig. 3 we show how the phase difference impacts on F for different valley splittings (here $E_v^R = E_v^L$). Whenever $E_v^R > E_Z^{R,L}/2$, $F > 80\%$ can be reached; in general we find a fidelity higher than 90% for $E_v \gtrsim 40t$. For a fixed valley splitting, the phase-dependence of F is non monotonic, as visible for small splittings ($E_v < 30\mu$eV). At low $\Delta\phi$ the fidelity is high because the intervalley anticrossing is very narrow and the two final states have different charge configurations over a large detuning range. The

minimum at $\Delta\phi \approx \frac{\pi}{2}$ arises from the opposite phase dependence of $t_{\pm\pm}$ and $t_{\pm\mp}$. Here a higher E_v^R is needed to realize a large energy separation between the two anticrossings in order to reach the same fidelity (see 90% contour line in Fig. 3). For $\Delta\phi > \frac{\pi}{2}$ the fidelity increases with increasing phase, since the increasing intervalley coupling is compensated by the smaller detuning needed for the $|\uparrow,\downarrow\rangle$ to evolve to $S_{(0,2)}^{--}$ (see Fig. 4). The decrease in F at high $\Delta\phi$ is due to the increase in the pulse diabaticity. The conversion fidelity in the adiabatic case shows that a fidelity higher than 90% can be reached even for $\Delta\phi \approx \pi$, as highlighted by the dotted red lines in Fig. 3, although it requires an impractical slow pulsing rate.

Properly tuning the readout position given a random phase difference is beneficial and enables to reach 99% fidelity threshold in a very large range of valley splittings and phase differences. The optimal readout point shifts with $\Delta\phi$ reflecting the state composition. As shown by the dots in Fig. 4, for a small phase difference it is convenient to readout close to the intervalley anticrossing, while for a large difference the pulse should end slightly beyond the intravalley anticrossing. In particular, the maximum fidelity is reached, as expected, for $\Delta\phi = 0$ and $\epsilon = E_v^R$ while a minimum arises at $\Delta\phi = \pi/2$. In Fig. 4 the fidelity is higher than 90% except where the level mixing is strong (e.g. $\epsilon \sim 0$ and $\Delta\phi \sim 0$ or $\epsilon \sim E_v^R$
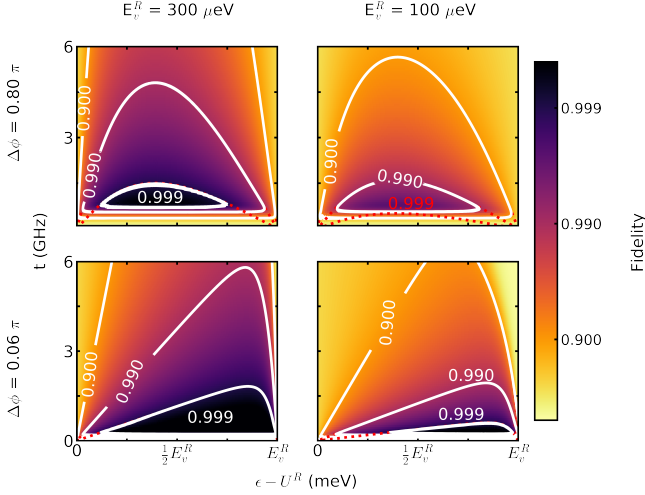
FIG. 5: Fidelity obtained by time evolution simulations (color map with white contour lines) and adiabatic pulses (red). A realistic value of 0.3 meV enables reaching $F > 99\%$ for t up to 4.5 GHz in a wide range of phase differences (here up to $\Delta\phi = 0.8\pi$). The reduction in fidelity at low t is caused by higher diabaticity of the pulse. In the top right panel it prevents reaching $F > 99.9\%$. As in Fig. 4 $\delta E_Z^- = 5$ MHz and the pulse extremes are $U^R \pm 2E_v^R$.

and $\Delta\phi \sim \pi$), but there are two separate regions where $F > 99.9\%$, because $E_v^R/t \sim 50$.
However, when aiming at $F > 99\%$ or higher, the control of the ancilla qubit valley splitting enables overcoming the low fidelity region at intermediate $\Delta\phi$. The two 99.9% regions merge for $E_v^R/t \sim 54$, e.g. when $t = 1.5$ GHz a valley splitting of at least 0.36 meV is required. Figure 5 shows that for experimentally obtained valley splitting high fidelity can be achieved for a quite large range of tunnel coupling t. For a valley splitting of 0.1 meV and considering perfect adiabatic pulses, a fidelity beyond 99.9% can be reached for $t \lesssim 500$ MHz and $0 \le \Delta\phi \le 0.7\pi$. When the valley splitting is slightly larger, i.e. 300 μeV, the same fidelity can be achieved for $t < 1.5$ GHz. When the valley splitting is 700 μeV, a fidelity of 99% can be reached when $t < 5$ GHz and a fidelity of 99.9% requires $t < 3$ GHz. Moreover, Fig. 5 shows that t could be used as an additional knob to improve the fidelity, in the case of limited control of the valley splitting.

IV. TRIPLE DOT READOUT PROTOCOL

Experimental works on Pauli-spin blockade in silicon quantum dots show readout fidelity significantly lower than the conversion fidelities reported here[38,39,42]. This reduction is predominantly due to the small sensitivity of the charge sensor to variations in the electric dipole caused by a difference in the charge position. Therefore protocols involving metastable states[38–40,42] have been
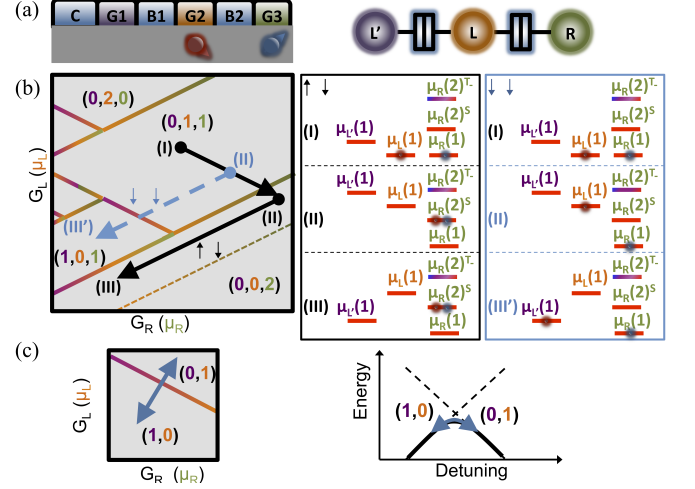

FIG. 6: (a) Schematic of a triple dot device with negligibly weak long-range coupling. (b) Left panel: Hysteretic stability diagram of a tripled quantum dot with the readout pulse scheme. The first step (from (I) to (II)) is a standard double-quantum dot Pauli-spin blockade readout pulse. In the second step (from (II) to (III)), charge moves from the target to the left ancilla qubit only if the target qubit is initially spin blocked (III'). Transitions between nearest neigbhoring dots are denoted by two-color interdot transition lines. The edges of the hysteresis regions are marked by three-color lines. The line color reflects the involved dots. Right panels: energy level diagrams showing the triple dot occupation at (I),(II), (III) and (III') positions for depending on the initial spin state. (c) Left panel: The readout is performed by oscillating the middle and left dot energy levels forcing the system to oscillates between the $(1,0,1)$ and $(0,1,1)$ charge states. Right panel: the charge states mixing leads to a capacitive term measured via rf gate-based dispersive readout. For simplicity, the charge occupation of the right dot is dropped since it remains constant.

proposed. Typically, after projecting the initial states onto a singlet $(0,2)$ or a triplet $(1,1)$, the system is pulsed deep in the $(0,2)$ region, past an excited charge state. While the singlet $(0,2)$ is still the ground state, the triplet $(1,1)$ relaxes (i.e. an electron tunnels from or to an electron reservoir) to the excited charge state. Coulomb blockade leads consequently to a long charge relaxation time. The variation in the sensor signal induced by a different number of electrons trapped in the double quantum dot is typically larger by a factor 1.4-4 and fidelities approaching 99.9% have been reported[38,39]. Furthermore, such latching mechanisms allow for delayed readout, splitting the spin-to-charge conversion from the actual readout process, which can be beneficial when scaling to large qubit arrays[14,16].

Here we replace the reservoir used in recent experimental works[38–40,42] with a third dot (L') added to the left side of the double dot considered in the previous Sections, providing clear benefits in scalability. In the following we consider that the triple dot is loaded with two electrons at the beginning of the protocol and then the coupling

to the electron reservoir is switched off. The triple dot is controlled by two "virtual" gates G_L and G_R, which are linear combinations of the B and G gates shown in Fig. 6a. In particular, defining μ_d the chemical potential of the dot d, we assume that $\mu_{L'}$ is kept to a reference level and that G_L shifts only μ_L. On the other hand, G_R is mainly coupled to μ_R, but controls also μ_L. The interdot transition lines with a positive(negative) slope in Fig. 6b correspond to $\mu_{L'(R)} = \mu_L$. We assume negligible long-range tunnel coupling $t^{RL'}$ between the two outer ancilla qubits (see Fig. 6a, right panel). This condition results in a stability diagram similar to the case of hysteretic double quantum dots[66]. The transition lines arising from direct tunneling between the ancilla qubits R and L' (e.g. the one between $(1,0,1)$ and $(0,0,2)$) are hysteretic and depend on the sweeping direction of the gate G_R. When $t^{RL'} \neq 0$ the condition $\mu_{L'} = \mu_R$ leads to electron transfer. The corresponding transition lines appear vertical in a stability diagram and are independent from G_L. However, when $t^{RL'} = 0$, tunneling can only occur when $\mu_{L'(R)} \geq \mu_L \geq \mu_{R(L')}$[39,66]. For increasing voltage G_R an electron can be transferred to R from L' when $\mu_{L'} = \mu_L \geq \mu_R$. Consequently, the lines have a negative slope. For decreasing G_R, transfer occurs when $\mu_R = \mu_L \geq \mu_{L'}$ and the slopes have positive slope, as in Fig. 6b.

The pulse protocol starts in a $(0,1,1)$ charge configuration, position (I) in Fig. 6b. Here $\mu_{L'}(1) > \mu_L(1), \mu_R(1)$. The system is detuned inside the $(0,0,2)$ spin-blocked window to position (II) where $\mu_{L'}(1), \mu_R(2)^{T^-} > \mu_L(1) > \mu_R(2)^S$. Here we assume that $\Delta\phi$, t, ϵ and E_v^R are optimized accordingly to the previous Sections to allow for high conversion fidelity. The initial state $(0, \uparrow, \downarrow)$ is then converted to a $(0,0,2)$ charge state, while $(0, \downarrow, \downarrow)$ remains blocked in a $(0,1,1)$ configuration. G_L and G_R are then lowered together, raising the chemical potentials μ_R and μ_L.

The detuning direction is parallel to the $(0,1,1) \leftrightarrow (0,0,2)$ charge transition line so that $\mu_R(2) < \mu_L(1)$ and their relative offset is kept constant. The pulse ends in the hysteretic $(0,0,2)$ region at position (III) where $\mu_{L'}(1) < \mu_R(2) < \mu_L(1)$, i.e. past the extension of the $(0,1,1) \leftrightarrow (1,0,1)$ transition line. The short-range coupling enables spin-to-charge conversion and charge shelving. If the separated spins were antiparallel, the $S_{(0,0,2)}$ will remain in the same charge configuration. This holds even for $\mu_{L'}(1) < \mu_R(2) < \mu_L(1)$, since no electrons can tunneling when $t^{RL'} = 0$. Parallel spins, however remain in the $(0,1,1)$ charge configuration. In that case, when $\mu_{L'}(1) = \mu_L(1)$ an electron is transferred between L and L'. As a consequence, $(0, \downarrow, \downarrow)$ and $(0, \uparrow, \downarrow)$ evolve to $(1,0,1)$ and $(0,0,2)$, respectively. The negligible long range tunnel coupling extends the spin flip relaxation time to a charge relaxation time, determined by cotunneling.

The next step of the protocol is the actual readout (Fig. 6c). First the tunnel coupling t^{LR} is completely switched off. The two possible final states of the $L'L$ double dot

are $(0,0)$ and $(1,0)$, if at the beginning of the pulse the two spins were, respectively, antiparallel or parallel. Now rf gate-based dispersive readout can be used. The presence or absence of an electron in the $L'L$ double dot can be translated with high fidelity to the spin state of the target qubit. We note that in the case of limited control of t^{LR} this scheme can still be implemented, since the rf tone is applied such that the system oscillates between $(1,0,1)$ and $(0,1,1)$. Importantly, the possibility to doubly occupy the left ancilla qubit softens the experimentally demanding requirements of the triple donor scheme of Ref. 67.

V. CONCLUSIONS

In summary, we have investigated the impact of an uncontrolled valley phase difference on the conversion fidelity of Pauli-spin blockade readout. The damping effect of the phase can be mitigated by the control of the valley splitting of the ancilla qubit. In particular, we have shown that the control of the valley splitting energy together with the optimization of the readout position is sufficient to overcome randomness of the valley phase difference, even when the control of the tunnel coupling is limited and t assumes realistic values. For $E_v^R > 0.3$ meV a fidelity higher than 99.9% can be reached for $t < 2$ GHz, as long as evolution is adiabatic with respect to the intravalley anticrossing. In addition, we have proposed a new protocol based on an isolated triple quantum dot to extend the Pauli-spin blockade readout measurement time by orders of magnitude, and significantly improving readout fidelity.

Our results show that the randomness of the valley phase difference can potentially lower the readout fidelity. However, the experimentally demonstrated control of valley splitting and fine tuning of the detuning can overcome such variability. The extended relaxation time obtainable in a triple dot protocol makes Pauli spin blockade thereby an excellent method to be integrated in large-scale spin qubit systems.

Appendix: Adiabaticity threshold

In this Appendix we discuss the adiabaticity condition for a linear pulse. For two level systems a detailed theory has been developed and the Landau-Zener formula[68,69] $p = \exp(-4\pi^2 t^2/hv)$ links the speed v of a linear pulse to the probability p of a diabatic transition between the eigenstates of the system. In the case of a multilevel system an analytical equation exists for the simple case of three-state ladder systems[70,71], where two states are differently coupled to a third state and which successfully describes coherent adiabatic passage[72] or stimulated Raman adiabatic passage[73].

Here we consider the three level system described by the

Hamiltonian:

$$H_{3L} = \begin{bmatrix} -\delta E_Z^-/2 & 0 & t_{--} \\ 0 & \delta E_Z^-/2 & -t_{--} \\ t_{--}^* & -t_{--}^* & U_o^R - \epsilon \end{bmatrix} \qquad (A.1)$$

written on the basis $[|\uparrow,\downarrow\rangle, |\downarrow,\uparrow\rangle, S_{(0,2)}]$. It approximates the 30-level system considered in the main close to the lowest valley branch intravalley anticrossing ($\epsilon \sim U^R$). Each of the three eigenstates $\Psi_{1,2,3}$ of H_{3L} undergoes an adiabatic evolution when the criterion[74]

$$\left| \frac{\alpha_i^{\max}}{\omega_i^{\min}} \right|^2 \ll 1 \qquad (A.2)$$

is satisfied. Here ω_i^{min} is the minimum energy difference between the i-th eigenstate and the closest neighbour, while α_i^{max} can be seen as the maximum "angular velocity"[74] of the state Ψ_i since it is defined as

$$|\alpha_i(t)|^2 = \sum_{j \neq i} |\alpha_{ij}(t)|^2 = \sum_{j \neq i} |\langle \dot{\Psi}_i(t)|\Psi_j(t)\rangle|^2. \qquad (A.3)$$

It has been shown (Ref. 74 for more details) that the total diabatic probability p_i during the time evolution of the i-th eigenstate satisfies

$$p_i \lesssim \max\left(\sum_{j \neq i} \left| \frac{\alpha_{ij}(t)}{\omega_{ij}(t)} \right|^2 \right) < p_i^{\max} = \left| \frac{\alpha_i^{\max}}{\omega_i^{\min}} \right|^2. \qquad (A.4)$$

From Eq. A.4 the dependency of p_i on the pulse speed can be obtained. Since for a linear pulse the speed $v = \dot{\epsilon}$ is constant we can rewrite $\dot{\Psi}_i(t)$ as $\dot{\Psi}_i(t) = \frac{\partial \Psi(t)}{\partial \epsilon} v$. An upper bound to the diabaticity probability is obtained by converting the inequality in Eq. A.4 to

$$p_i = v^2 \max\left(\sum_{j \neq i} \left| \frac{\tilde{\alpha}_{ij}(t)}{\omega_{ij}(t)} \right|^2 \right), \qquad (A.5)$$

where $\tilde{\alpha}_{ij}(t)$ is the speed-normalized "angular velocity". Equation A.5 can be used as a lower bound for the speed to obtain a defined p_i.

In Fig. 7a $\tilde{\alpha}_1$ is plotted, as well as the two contributions $\tilde{\alpha}_{12}$ and $\tilde{\alpha}_{13}$, as a function of the detuning. At negative detuning the dominant term is $\tilde{\alpha}_{12}$ meaning that the Zeeman energy difference sets the adiabaticity condition; while $\tilde{\alpha}_{13}$ better describes the system around zero detuning. For the particular case shown in Fig. 7 of $t_{--} = 1.5$ GHz and $\delta E_Z = 10$ MHz the peak at zero detuning is lower than the one related to the Zeeman energy difference. In such a scenario, it is possible to adiabatically pulse from $S_{(0,2)}$ to $|\uparrow,\downarrow\rangle$, defining the adiabaticity with respect to the tunnel coupling only, given a large detuning range and a small p_1. For higher tunnel coupling the zero-detuning peak becomes dominant and the two-level approximation becomes more accurate.

Eq. A.5 can be used to set the speed of a Pauli-spin blockade pulse in such a way that pulses with different t
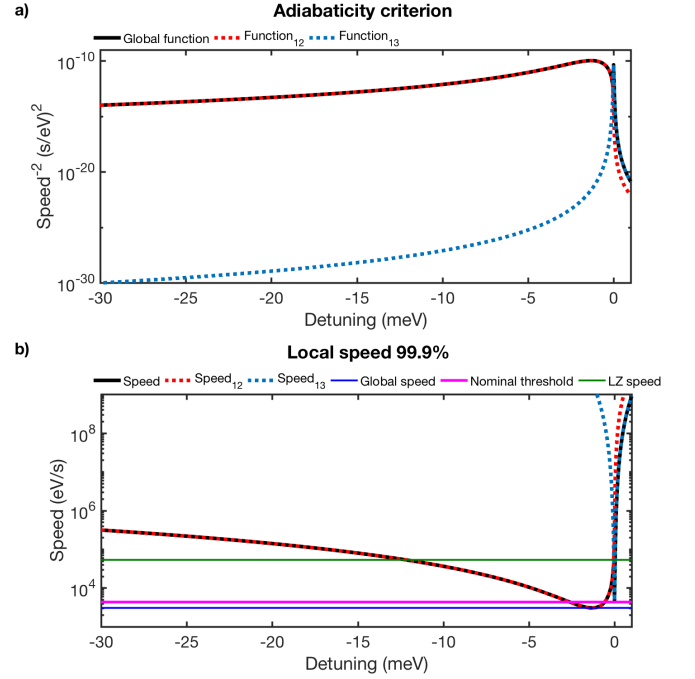

FIG. 7: a) The speed-normalized "angular velocity" $\tilde{\alpha}_1$ of the ground state as a function of the detuning. At negative detuning it reduces to $\tilde{\alpha}_{12}$, while at positive to $\tilde{\alpha}_{13}$. Here t = 1.5 GHz, $\delta E_Z = 10$ MHz and $\Delta\phi = 0$. The peak at the anticrossing correspond to the contribution of a pure two-level system, while the broad peak is due to the fact that $|\uparrow,\downarrow\rangle$ and $|\downarrow,\uparrow\rangle$ are coupled to each other only via the singlet (0,2). b) The "99.9% adiabatic probability" local speed as a function of detuning. The lower and upper horizontal lines are the global speed obtained using Eq. A.2 and the Landau-Zener formula, respectively. The middle one stems for the global 99.8% global probability speed.

satisfy the same adiabaticity condition. The function to be maximized in the right-hand side of Eq. A.5 can be viewed as a "local" speed since it is a function of time and thus detuning. As shown in Fig. 7b, it has the same trend as $\tilde{\alpha}_1$ and can be analogously split in two contributions. While the speed obtained from Eq. A.5 corresponds tot the global minimum of the "local" speed, the global speed calculated from $p_i^{\max}$ is orders of magnitude smaller. Since $p_i^{\max}$ is an upper bound, using this definition will make the pulses much slower than what is required, and the use of p_i allows for faster pulses. The fidelity of a $|\uparrow,\downarrow\rangle \rightarrow S_{(0,2)}$ pulse is limited by the adiabaticity of the charge transition, therefore the higher the adiabaticity the higher the fidelity. In general, the global speed derived using the Landau-Zener formula for $p = 0.1\%$ would result in a fidelity approaching 99.9%, while setting $p_i = 0.2$ in Eq. A.5 or replacing t with $t/2$ in the Landau-Zener formula allows for fidelity higher than 99.9%.

In the time evolution shown in Fig. 2d a linear pulse from $\epsilon = 0$ to $\epsilon = U^R + 2E_v^R$, with the $p_i = 0.2$ approximation, was used.

Appendix: Valley mixing Hamiltonian

Although the valley degree of freedom can be regarded as a pseudospin, there are some differences between the case of silicon bulk valleys and a single spin in a magnetic field. The general Hamiltonian of a spin 1/2 in a magnetic field has three parameters, i.e. the three components of the magnetic fields, and the mixing perturbation is fully described by two angles and the magnitude. The particular case of the silicon z bulk valleys can be derived from the general case by setting the z-component of the (effective) magnetic field (diagonal terms of the Hamiltonian) to zero. As demonstrated by early works on valley physics in silicon[21–23], the six-fold degeneracy of the conduction band is first split by confinement, which lifts the x and y valleys leaving the degeneracy between the z and $-z$ bulk (or bare) valleys. The remaining degeneracy is lifted by the electric field in the z direction and the interface (and a small contribution from the magnetic field). This perturbation (V_v) has the same effect on the two $\pm z$ valleys. The valley mixing Hamiltonian written in the basis spanned by the bulk valley states has equal diagonal terms, i.e. $\langle D_z|V_v|D_z\rangle = \langle D_{-z}|V_v|D_{-z}\rangle = \Lambda$. The effective valley Hamiltonian thus reads:

$$H_v = \begin{bmatrix} \Lambda & \Delta_v \\ \Delta_v^* & \Lambda \end{bmatrix} \qquad (A.1)$$

As a result, the offset Λ can be extracted and included in the orbital energy and the mixing of the bulk valleys is fully described by the complex number Δ_v[32]. By rewriting H_v in the eigenstate basis ($D_\pm$) Eq. 1 of the main is obtained.

Acknowledgments

* Electronic address: m.l.v.tagliaferri@tudelft.nl
† Electronic address: m.veldhorst@tudelft.nl

[1] M. Veldhorst, J. Hwang, C. Yang, A. Leenstra, B. de Ronde, J. Dehollain, J. Muhonen, F. Hudson, K. Itoh, A. Morello, et al., Nature Nanotechnology **9**, 981 (2014).

[2] J. Yoneda, K. Takeda, T. Otsuka, T. Nakajima, M. R. Delbecq, G. Allison, T. Honda, T. Kodera, S. Oda, Y. Hoshi, et al., Nature Nanotechnology **13**, 102 (2018).

[3] M. Veldhorst, C. H. Yang, J. C. C. Hwang, W. Huang, J. P. Dehollain, J. T. Muhonen, S. Simmons, A. Laucht, F. E. Hudson, K. M. Itoh, et al., Nature **526**, 410 (2015).

[4] D. M. Zajac, A. Sigillito, M. Russ, F. Borjans, J. Taylor, G. Burkard, and J. Petta, Science **359**, 439 (2018).

[5] T. F. Watson, S. G. J. Philips, E. Kawakami, D. R. Ward, P. Scarlino, M. Veldhorst, D. E. Savage, M. G. Lagally, M. Friesen, S. N. Coppersmith, et al., Nature **555**, 633 (2018).

[6] D. Loss and D. P. DiVincenzo, Physical Review A **57**, 120 (1998).

[7] B. E. Kane, Nature **393**, 133 (1998).

[8] J. Taylor, H.-A. Engel, W. Dür, A. Yacoby, C. Marcus, P. Zoller, and M. Lukin, Nature Physics **1**, 177 (2005).

[9] K. D. Petersson, L. W. McFaul, M. D. Schroer, M. Jung, J. M. Taylor, A. A. Houck, and J. R. Petta, Nature **490**, 380 (2012).

[10] C. D. Hill, E. Peretz, S. J. Hile, M. G. House, M. Fuechsle, S. Rogge, M. Y. Simmons, and L. C. Hollenberg, Science Advances **1**, e1500707 (2015).

[11] G. Pica, B. W. Lovett, R. N. Bhatt, T. Schenkel, and S. A. Lyon, Physical Review B **93**, 035306 (2016).

[12] G. Tosi, F. A. Mohiyaddin, V. Schmitt, S. Tenberg, R. Rahman, G. Klimeck, and A. Morello, Nature Communications **8**, 450 (2017).

[13] T. A. Baart, T. Fujita, C. Reichl, W. Wegscheider, and L. M. K. Vandersypen, Nature nanotechnology **12**, 26 (2017).

[14] R. Li, L. Petit, D. P. Franke, J. P. Dehollain, J. Helsen, M. Steudtner, N. K. Thomas, Z. R. Yoscovits, K. J. Singh, S. Wehner, et al., arXiv:1711.03807 (2017).

[15] L. M. K. Vandersypen, H. Bluhm, J. S. Clarke, A. S. Dzurak, R. Ishihara, A. Morello, D. J. Reilly, L. R. Schreiber, and M. Veldhorst, npj Quantum Information **3**, 34 (2017).

[16] M. Veldhorst, H. Eenink, C. Yang, and A. Dzurak, Nature Communications **8** (2017).

[17] J. Helsen, M. Steudtner, M. Veldhorst, and S. Wehner, Quantum Science and Technology **3**, 035005 (2018).

[18] F. A. Zwanenburg, A. S. Dzurak, A. Morello, M. Y. Simmons, L. C. Hollenberg, G. Klimeck, S. Rogge, S. N. Coppersmith, and M. A. Eriksson, Reviews of Modern Physics **85**, 961 (2013).

[19] C. Yang, A. Rossi, R. Ruskov, N. Lai, F. Mohiyaddin, S. Lee, C. Tahan, G. Klimeck, A. Morello, and A. Dzurak, Nature Communications **4**, 2069 (2013).

[20] J. K. Gamble, M. A. Eriksson, S. N. Coppersmith, and M. Friesen, Physical Review B **88**, 035310 (2013).

[21] M. Friesen and S. N. Coppersmith, Physical Review B **81**, 115324 (2010).

[22] D. Culcer, X. Hu, and S. D. Sarma, Physical Review B **82**, 205315 (2010).

[23] M. Friesen, S. Chutia, C. Tahan, and S. N. Coppersmith, Physical Review B **75**, 115318 (2007).

[24] For a detailed analysis on the boundary conditions for these assumptions we refer to Ref. 32.

[25] J. S. Schoenfield, B. M. Freeman, and H. Jiang, Nature Communications **8**, 64 (2017).

[26] W. Lim, C. Yang, F. Zwanenburg, and A. Dzurak, Nanotechnology **22**, 335704 (2011).

[27] C. H. Yang, W. H. Lim, N. S. Lai, A. Rossi, A. Morello, and A. S. Dzurak, Physical Review B **86**, 115319 (2012).

[28] E. Kawakami, P. Scarlino, D. Ward, F. Braakman, D. Savage, M. Lagally, M. Friesen, S. Coppersmith, M. Eriksson, and L. Vandersypen, Nature Nanotechnology **9**, 666 (2014).

[29] N. Rohling and G. Burkard, New Journal of Physics **14**, 083008 (2012).

[30] Y. Wu and D. Culcer, Physical Review B **86**, 035321 (2012).

[31] M. J. Calderón, B. Koiller, and S. DasSarma, Physical Review B **77**, 155302 (2008).

[32] N. M. Zimmerman, P. Huang, and D. Culcer, Nano Letters **17**, 4461 (2017).

[33] J. Petta, A. C. Johnson, J. Taylor, E. Laird, A. Yacoby, M. D. Lukin, C. Marcus, M. Hanson, and A. Gossard, Science **309**, 2180 (2005).

[34] B. Maune, M. Borselli, B. Huang, T. Ladd, P. Deelman, K. Holabird, A. Kiselev, I. Alvarado-Rodriguez, R. Ross, A. Schmitz, et al., Nature **481**, 344 (2012).

[35] A. Johnson, J. Petta, J. Taylor, A. Yacoby, M. Lukin, C. Marcus, M. Hanson, and A. Gossard, Nature **435**, 925 (2005).

[36] J. R. Petta, A. C. Johnson, A. Yacoby, C. M. Marcus, M. P. Hanson, and A. C. Gossard, Physical Review B **72**, 161301 (2005).

[37] R. Hanson, L. Kouwenhoven, J. Petta, S. Tarucha, and L. Vandersypen, Reviews of Modern Physics **79**, 1217 (2007).

[38] M. Fogarty, K. Chan, B. Hensen, W. Huang, T. Tanttu, C. Yang, A. Laucht, M. Veldhorst, F. Hudson, K. Itoh, et al., arXiv:1708.03445 (2017).

[39] P. Harvey-Collard, B. D'Anjou, M. Rudolph, N. T. Jacobson, J. Dominguez, G. A. T. Eyck, J. R. Wendt, T. Pluym, M. P. Lilly, W. A. Coish, et al., arXiv:1703.02651 (2017).

[40] S. Studenikin, J. Thorgrimson, G. Aers, A. Kam, P. Zawadzki, Z. Wasilewski, A. Bogan, and A. Sachrajda, Applied Physics Letters **101**, 233101 (2012).

[41] B. Chen, B. Wang, G. Cao, H. Li, M. Xiao, and G. Guo, Science Bulletin **62**, 712 (2017).

[42] T. Nakajima, M. R. Delbecq, T. Otsuka, P. Stano, S. Amaha, J. Yoneda, A. Noiri, K. Kawasaki, K. Takeda, G. Allison, et al., Physical Review Letters **119**, 017701 (2017).

[43] M. Veldhorst, R. Ruskov, C. H. Yang, J. C. C. Hwang, F. E. Hudson, M. E. Flatté, C. Tahan, K. M. Itoh, A. Morello, and A. S. Dzurak, Physical Review B **92**, 201401 (2015).

[44] R. M. Jock, N. T. Jacobson, P. Harvey-Collard, A. M. Mounce, V. Srinivasa, D. R. Ward, J. Anderson, R. Manginell, J. R. Wendt, M. Rudolph, et al., Nature Communications **9**, 1768 (2018).

[45] R. Ferdous, K. W. Chan, M. Veldhorst, J. Hwang, C. Yang, G. Klimeck, A. Morello, A. S. Dzurak, and R. Rahman, arXiv:1703.03840 (2017).

[46] R. Ferdous, E. Kawakami, P. Scarlino, M. P. Nowak, D. Ward, D. Savage, M. Lagally, S. Coppersmith, M. Friesen, M. A. Eriksson, et al., arXiv:1702.06210 (2017).

[47] R. Ruskov, M. Veldhorst, A. S. Dzurak, and C. Tahan, arXiv:1708.04555 (2017).

[48] A. L. Saraiva, M. J. Calderón, R. B. Capaz, X. Hu, S. D. Sarma, and B. Koiller, Physical Review B **84**, 155320 (2011).

[49] D. Culcer, Ł. Cywiński, Q. Li, X. Hu, and S. D. Sarma, Physical Review B **82**, 155312 (2010).

[50] A. L. Saraiva, M. J. Calderón, X. Hu, S. DasSarma, and B. Koiller, Physical Review B **80**, 081305 (2009).

[51] M. Friesen, M. Eriksson, and S. Coppersmith, Applied physics letters **89**, 202106 (2006).

[52] L. Jiang, C. H. Yang, Z. Pan, A. Rossi, A. S. Dzurak, and D. Culcer, Physical Review B **88**, 085311 (2013).

[53] Y. Hada and M. Eto, Physical Review B **68**, 155322 (2003).

[54] Q. Li, Ł. Cywiński, D. Culcer, X. Hu, and S. D. Sarma, Physical Review B **81**, 085313 (2010).

[55] G. Burkard and J. R. Petta, Physical Review B **94**, 195305 (2016).

[56] X. Mi, C. G. Péterfalvi, G. Burkard, and J. R. Petta, Physical Review Letters **119**, 176803 (2017).

[57] A. Crippa, M. L. V. Tagliaferri, D. Rotta, M. De Michielis, G. Mazzeo, M. Fanciulli, R. Wacquez, M. Vinet, and E. Prati, Physical Review B **92**, 035424 (2015).

[58] A. C. Betz, R. Wacquez, M. Vinet, X. Jehl, A. L. Saraiva, M. Sanquer, A. J. Ferguson, and M. F. Gonzalez-Zalba, Nano Letters **15**, 4622 (2015).

[59] K. Petersson, C. Smith, D. Anderson, P. Atkinson, G. Jones, and D. Ritchie, Nano letters **10**, 2789 (2010).

[60] R. Mizuta, R. M. Otxoa, A. C. Betz, and M. F. Gonzalez-Zalba, Physical Review B **95**, 045414 (2017).

[61] L. E. Golub and E. L. Ivchenko, Physical Review B **69**, 115333 (2004).

[62] M. O. Nestoklon, L. E. Golub, and E. L. Ivchenko, Physical Review B **73**, 235334 (2006).

[63] M. O. Nestoklon, E. L. Ivchenko, J.-M. Jancu, and P. Voisin, Physical Review B **77**, 155328 (2008).

[64] W. Huang, M. Veldhorst, N. M. Zimmerman, A. S. Dzurak, and D. Culcer, Physical Review B **95**, 075403 (2017).

[65] J. M. Taylor, J. R. Petta, A. C. Johnson, A. Yacoby, C. M. Marcus, and M. D. Lukin, Physical Review B **76**, 035315 (2007).

[66] C. Yang, A. Rossi, N. Lai, R. Leon, W. Lim, and A. Dzurak, Applied Physics Letters **105**, 183505 (2014).

[67] A. D. Greentree, A. R. Hamilton, L. C. L. Hollenberg, and R. G. Clark, Physical Review B **71**, 113310 (2005).

[68] S. Shevchenko, S. Ashhab, and F. Nori, Physics Reports **492**, 1 (2010).

[69] N. V. Vitanov and B. M. Garraway, Physical Review A **53**, 4288 (1996).

[70] C. Carroll and F. Hioe, Journal of physics A: mathematical and general **19**, 1151 (1986).

[71] N. V. Vitanov, T. Halfmann, B. W. Shore, and K. Bergmann, Annual review of physical chemistry **52**, 763 (2001).

[72] A. D. Greentree, J. H. Cole, A. R. Hamilton, and L. C. L. Hollenberg, Physical Review B **70**, 235317 (2004).

[73] N. V. Vitanov, A. A. Rangelov, B. W. Shore, and K. Bergmann, Reviews of Modern Physics **89**, 015006 (2017).

[74] A. Messiah, *Quantum mechanics. vol. i..* (1958).